A Multiscale Numerical Study of Hurricane Andrew (1992). Part III: Dynamically Induced Vertical Motion

DA-LIN ZHANG

Department of Meteorology, University of Maryland, College Park, Maryland

YUBAO LIU

NCAR/RAP, Boulder, Colorado

M. K. YAU

Department of Atmospheric and Oceanic Sciences, McGill University, Montreal, Quebec, Canada

(Manuscript received 24 June 1999, in final form 3 April 2000)

ABSTRACT

In this study, the vertical force balance in the inner-core region is examined, through the analysis of vertical momentum budgets, using a high-resolution, explicit simulation of Hurricane Andrew (1992). Three-dimensional buoyancy- and dynamically induced perturbation pressures are then obtained to gain insight into the processes leading to the subsidence warming in the eye and the vertical lifting in the eyewall in the absence of positive buoyancy.

It is found from the force balance budgets that vertical acceleration in the eyewall is a small difference among the perturbation pressure gradient force (PGF), buoyancy, and water loading. The azimuthally averaged eyewall convection is found to be conditionally stable but slantwise unstable with little positive buoyancy. It is the PGF that is responsible for the upward acceleration of high-θ_e air in the eyewall. It is found that the vertical motion and acceleration in the eyewall are highly asymmetric and closely related to the azimuthal distribution of radial flows in conjunction with large thermal and moisture contrasts across the eyewall. For example, the radially incoming air aloft is cool and dry and tends to suppress updrafts or induce downdrafts. On the other hand, the outgoing flows are positively buoyant and tend to ascend in the eyewall unless evaporative cooling dominates. It is also found that the water loading effect has to be included into the hydrostatic equation in estimating the pressure or height field in the eyewall.

The perturbation pressure inversions show that a large portion of surface perturbation pressures is caused by the moist-adiabatic warming in the eyewall and the subsidence warming in the eye. However, the associated buoyancy-induced PGF is mostly offset by the buoyancy force, and their net effect is similar in magnitude but opposite in sign to the dynamically induced PGF. Of importance is that the dynamically induced PGF points downward in the eye to account for the maintenance of the general descent. But it points upward in the outer portion of the eyewall, particularly in the north semicircle, to facilitate the lifting of high-θ_e air in the lower troposphere. Furthermore, this dynamic force is dominated by the radial shear of tangential winds. Based on this finding, a new theoretical explanation, different from previously reported, is advanced for the relationship among the subsidence warming in the eye, and the rotation and vertical wind shear in the eyewall.

1. Introduction

Despite considerable research in tropical storms during the past five decades, conflicting views on the inner-core dynamics of hurricanes still remain due to the lack of complete, high-resolution, and dynamically consistent datasets. One controversy concerns the dynamical and physical processes leading to the subsidence warming in the eye and the intense updrafts in the eyewall. Since the intensity and changes in intensity of hurricanes are closely related to the vertical motion and its associated secondary circulations in the inner-core region, it is extremely important to understand the dynamics involved in their development and their relation to the primary circulations of the storms.

Earlier theoretical studies suggested that the weak subsidence in the eye is caused by radially outward advection of the eye air into the eyewall as a result of supergradient flows in the inner-core region (Malkus 1958; Kuo 1959). The existence of supergradient flows

Corresponding author address: Dr. Da-Lin Zhang, Department of Meteorology, University of Maryland, College Park, MD 20742-2425.
E-mail: dalin@atmos.umd.edu

in a deep layer, particularly near the radius of maximum winds (RMW), has been found by Gray and Shea (1973) from a composite analysis of many radial legs of flight data. However, other observational studies indicated that gradient wind balance is a good approximation to the azimuthally averaged tangential winds above the boundary layer and below the upper outflow layer (e.g., Willoughby 1990). The unbalanced flow will be a separate subject for Part IV of this series of papers.

Using an axisymmetric vortex model, Smith (1980) demonstrated that the subsidence warming in the eye is mechanically driven by the decreased vertical shear in tangential winds in the eyewall as a consequence of thermal wind balance. Specifically, the radial pressure drop from the outer edge to the center of the eye is determined by the rotation in the eyewall via gradient wind balance. Because the tangential winds in the eyewall decrease with height, the radial pressure drop must decrease upward, inducing subsidence and giving rise to a temperature maximum at the eye center. This implicitly implies that the warm-cored eye is a result of the development of negative vertical shear in the eyewall. According to Smith (1980), the supergradient flows should also be expected in the inner-core region in order for the subsiding air to flow outward.

In contrast, Shapiro and Willoughby (1982) viewed the descent in the eye as compensational subsidence associated with vigorous convection in the eyewall. The air mass in the eyewall would detrain at the top, sink into the eye, and flow back into the eyewall at the bottom. The idea of subsidence caused by the eyewall convection was questioned by Emanuel (1997). He used a balance model to demonstrate that the convectively induced subsidence cannot by itself raise the vertically averaged temperature in the eye to the values greater than that inside the eyewall. He proposed that the amplification of the swirling flow is strongly frontogenetic, and it would lead to a thermal and momentum discontinuity at the inner edge of the eyewall. This discontinuity may collapse and cause the radial turbulent diffusion of momentum, thereby inducing mechanically a secondary circulation with the descending motion in the eye. Willoughby (1998) argued that such a collapse may be prevented by mixing. Meanwhile, he modified the conceptual model of Shapiro and Willoughby (1982), based on the analyses of soundings taken at the center of some hurricanes, and suggested that the descending air above an inversion (at an altitude of 2–3 km) in the eye has been there since the eye is first formed. As the storm deepens, the slow descent in the eye, occurring at a few centimeters per second, represents the response to the net mass loss caused by the moist downward cascade inside the eye and the convective updrafts in the eyewall above the inversion. This observational finding was recently confirmed by the high-resolution simulation of Hurricane Andrew (1992); see Figs. 5 and 6 in Liu et al. (1999).

There have also been different opinions on the role of convective available potential energy (CAPE) or buoyancy energy in the development of intense updrafts in the eyewall. Gray and Shea (1973) showed the existence of considerable potential instability in the ambient environment as well as pronounced CAPE in the eyewall. Similar findings were also reported in other observational studies (e.g., Ebert and Holland 1992; Black et al. 1994). Moreover, almost all of the early idealized simulations of tropical storms began with very unstable soundings (e.g., Ooyama 1969; Anthes 1972; Kurihara and Tuleya 1981), being motivated by the assumptions associated with the theory of conditional instability of the second kind (CISK). Because cumulus parameterizations were used in these simulations, positive CAPE should be expected in the simulated (upright) eyewall/spiral rainbands.

A dramatically different view of hurricane development was presented by Emanuel (1986), who hypothesized that hurricanes develop from air–sea interaction involving a positive feedback between a finite-amplitude vortex and the wind-induced sensible and latent heat fluxes from the underlying warm ocean. Subsequently, Rotunno and Emanuel (1987) demonstrated with an axisymmetric cloud model that a hurricane could spin up when ambient CAPE is absent in the initial conditions. Emanuel's idea differs from the earlier concept of CISK in that deep convection redistributes the sensible and latent heat from the ocean surface such that the moist ascent in the eyewall becomes locally neutral to slantwise convection. It implies that slantwise convective available potential energy (SCAPE) should be very small in the eyewall, particularly during the mature stage. Therefore, hurricanes are not thermodynamically driven as are other types of mesoscale convective systems.

The purpose of this study is to examine the different views presented above via the vertical momentum budget and the inverted three-dimensional (3D) perturbation pressures in the inner-core region of a hurricane. This study will be done using a 72-h, triply nested, fully explicit, high-resolution ($\Delta x = 6$ km) simulation of Hurricane Andrew (1992) with the state-of-the-art Pennsylvania State University–National Center for Atmospheric Research (NCAR) nonhydrostatic Mesoscale Model (MM5). Specifically, Liu et al. (1997, 1999, hereafter referred to as Parts I and II, respectively), have shown that MM5 reproduces well the track and intensity, the structures of the eye, eyewall, spiral rainbands, RMW, and other inner-core features as compared to available observations and the results of previous hurricane studies. Thus, the simulation provides a four-dimensional, dynamically consistent dataset to examine the inner-core dynamics of a model hurricane. In this study, we attempt to address the following questions: *What dynamical processes are responsible for the weak descent in the eye? Is the warming in the eye caused by the negative vertical shear in the eyewall or vice versa? Is there any relationship between the secondary*

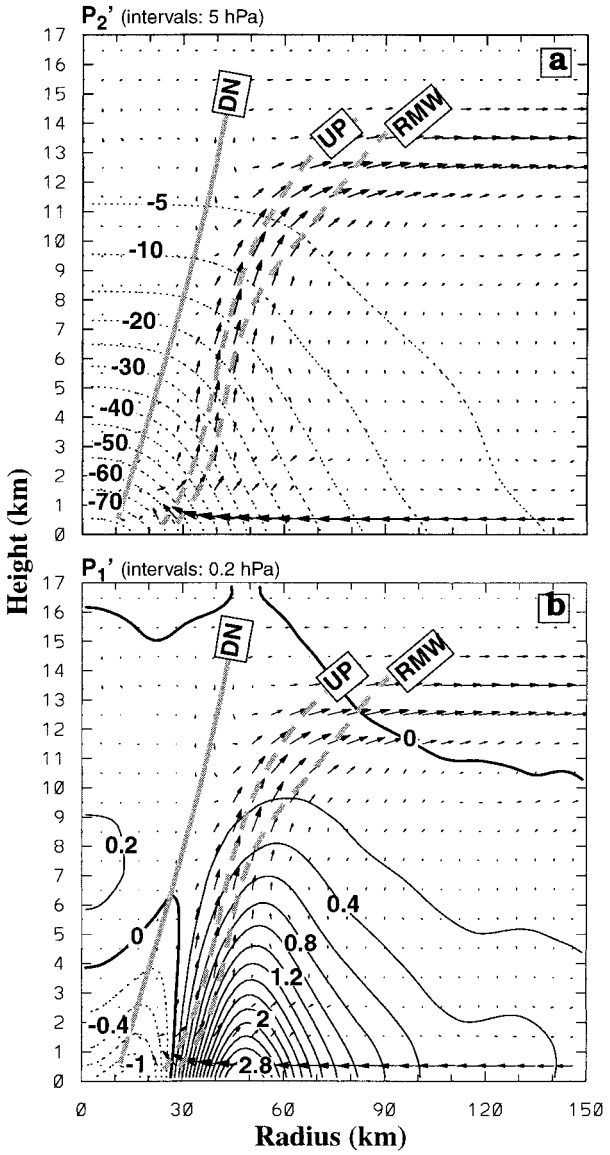

FIG. 1. Radius–height cross sections of the hourly and azimuthally averaged (a) perturbation pressure p_2' at intervals of 5 hPa and (b) perturbation pressure p_1' (see the text for definition) that are obtained from 12 model outputs at 5-min intervals during the 1-h budget period ending at 2100 UTC 23 Aug 1992. Solid (dashed) lines are positive (negative) values. Axes of downdrafts (DN), updrafts (UP), and the RMW, determined from Fig. 2, are also given, similarly for the rest of figures.

and the primary circulations of hurricanes? Is there any pronounced CAPE or SCAPE in a rapidly deepening hurricane like Andrew? How would the eyewall convection be driven in the absence of positive CAPE?

This paper is organized as follows. The next section presents procedures to compute the vertical momentum budget in cylindrical coordinates and shows some axisymmetric structures of the storm. Section 3 describes the vertical momentum budget. Section 4 (and the appendix) shows how the 3D buoyancy and dynamic per-

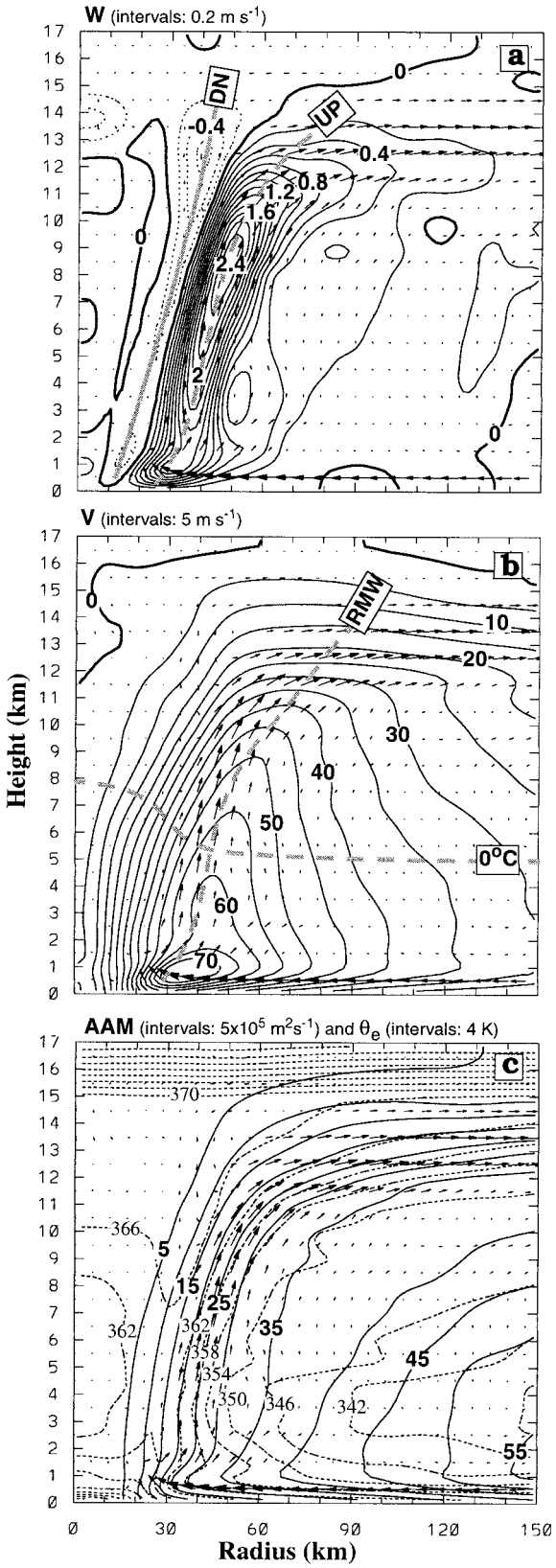

FIG. 2. As in Fig. 1 but for (a) vertical velocity (W) at intervals of 0.2 m s^{-1}, (b) tangential winds (V) at intervals of 5 m s^{-1}, and

turbation pressures are obtained for various source terms. It also addresses the nature of dynamically driven vertical motion in the eye and eyewall. An alternative theory, based on the pressure fields obtained from an inversion procedure, is proposed to explain the relationship among the warming in the eye, the rotation, and the vertical wind shear in the eyewall. A summary and concluding remarks are given in the final section.

2. Analysis procedures and inner-core structures

In the MM5 model (see Dudhia 1993; Grell et al. 1995), all prognostic variables are written in the mass-weighted (i.e., $p^* = p_s - p_t$) flux form with a vertical σ coordinate on a Mercator map projection, where p_s and p_t are the pressure at the bottom and the top of the model, respectively. Like most nonhydrostatic models, a reference state that varies only with height is defined. The buoyancy and pressure perturbations relative to the basic state are then used to compute the vertical acceleration in the vertical momentum equation. It is obvious that the perturbation quantities depend on the choice of the basic state. To obtain a realistic local buoyancy and perturbation pressure in our budget analysis, we define a three-dimensional reference state ($\overline{p}$, $\overline{T_v}$, $\overline{\rho}$) as follows. First, a reference virtual temperature field ($\overline{T_v}$) is obtained by performing a running average of the model output data using four neighboring points on constant σ surfaces. Second, a reference pressure ($\overline{p}$) is calculated by integrating the hydrostatic equation using $\overline{T_v}$. The reference-state variables are therefore a function of (x, y, σ, t). The perturbation pressure, perturbation virtual temperature, and perturbation air density are then given by

$$p'(x, y, \sigma, t) = p(x, y, \sigma, t) - \overline{p}(x, y, \sigma, t), \quad (1a)$$

$$T_v'(x, y, \sigma, t) = T_v(x, y, \sigma, t) - \overline{T_v}(x, y, \sigma, t), \quad (1b)$$

$$\rho'(x, y, \sigma, t) = \rho(x, y, \sigma, t) - \overline{\rho}(x, y, \sigma, t). \quad (1c)$$

Because mature hurricanes are predominantly axisymmetric, it is convenient to discuss the inner-core dynamics in cylindrical coordinates (r, λ, z), where r is the radius from the vortex's minimum pressure pointing outward, λ is the azimuthal angle, and z is the vertical height; see section 2 in Part II for a detailed description of the transformation between the MM5 (x, y, σ) coordinates and the cylindrical coordinates. The vertical momentum equation following a parcel in cylindrical coordinates is given below:

$$\frac{dW}{dt} = -\frac{1}{\rho}\frac{\partial p'}{\partial z} + g\left(\frac{\overline{\rho}}{\rho}\frac{T_v'}{T_v} - \frac{p'}{p}\right) - g(q_c + q_r + q_i + q_s + q_g) + 2\Omega u_m \cos\phi + D_w, \quad (2)$$

where

$$\frac{d}{dt} = \frac{\partial}{\partial t} + U\frac{\partial}{\partial r} + \frac{V}{r}\frac{\partial}{\partial \lambda} + W\frac{\partial}{\partial z}, \quad (3)$$

with W, U, and V being the respective vertical, radial, and tangential winds in cylindrical coordinates. The variables q_c, q_r, q_i, q_s, and q_g are the mixing ratio of cloud water, rainwater, cloud ice, snow, and graupel, respectively. The latitude is denoted by ϕ and D_w represents the vertical and horizontal diffusion. Note that the x component of the horizontal wind u_m is actually the projections of U and V onto the zonal axis and it is the zonal component of MM5's horizontal flow in Mercator projection. Equation (2) states that the vertical acceleration following a parcel is determined by an imbalance among various forces on the right-hand side (rhs) including the vertical perturbation pressure gradient force (PGF, W_P); the local buoyancy force (W_B), which is further decomposed into the thermal (W_{BTV}) and dynamic (W_{BDP}) buoyancy relative to the ambient environment; the water loading (W_L); the Coriolis effects (W_C) due to the zonal flow; and the diffusion effects (W_D).

Since the effect of perturbation pressure is one of the main objects of this study, we present in Fig. 1 the axisymmetric perturbation pressures (p_1') obtained from an azimuthal average of p' in Eq. (1a). For comparison, we also define another basic-state pressure $\overline{p}(z, t)$, which is some horizontally averaged pressure discussed in the appendix. The azimuthally averaged perturbation pressure with respect to $\overline{p}(z, t)$ is denoted by p_2'. It is evident from Fig. 1a that p_2' exhibits a maximum surface pressure deficit of >80 hPa at the center of the storm and the magnitude decreases rapidly with height. In contrast, the magnitude of p_1' is one order of magnitude smaller and is positive in most places except at levels below 4 km in the eye. The maximum surface value amounts to about 3 hPa near the radius of 50 km. Of interest is the vertical distribution of p_1', which decreases with height in the eyewall and its outer region, but increases in the eye up to the peak warm-core level (i.e., an altitude of 7.5 km, see Fig. 3 in Part II). As will be shown in the next section, the local perturbation pressure p_1' and the local virtual temperature perturbation T_v' with respect to $\overline{p}(x, y, \sigma, t)$ and $\overline{T_v}(x, y, \sigma, t)$ provide a more intuitive and efficient description of the relationship between the vertical PGF (W_P) and local buoyancy force (W_B), and their role in governing the vertical acceleration in hurricanes.

Whenever available, the budget terms in Eq. (2) are obtained directly from the MM5 output over the fine-

←

(c) AAM at intervals of 5×10^5 m^2 s^{-1}, superimposed with in-plane wind vectors and equivalent potential temperature [i.e., dashed lines in (c), every 4 K].

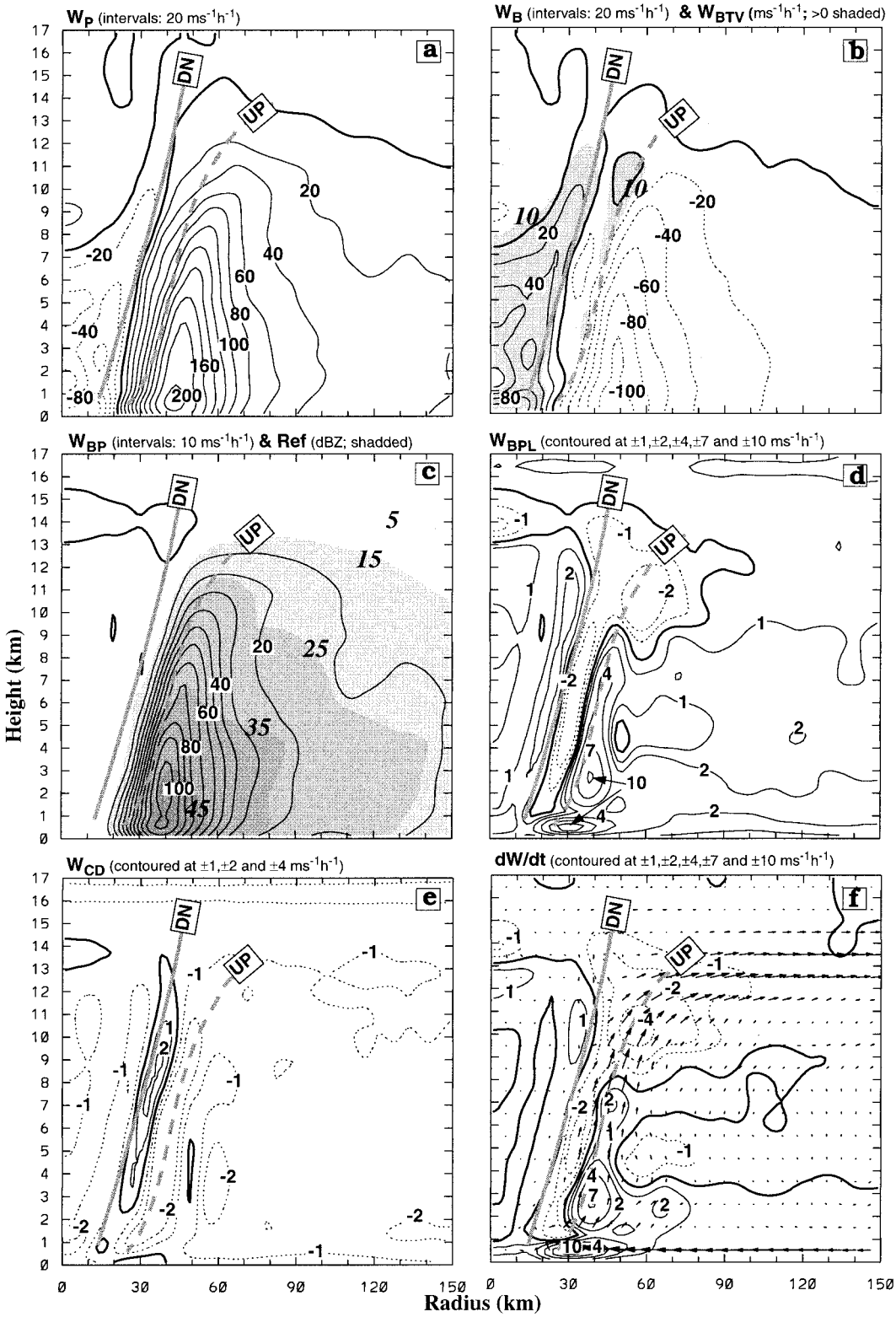

FIG. 3. As in Fig. 1 but for the vertical momentum budget: (a) the perturbation PGF (W_P), (b) the buoyancy force (W_B) with its positive thermal component shaded at 0 and 10 m s^{-1} h^{-1}, (c) $W_{BP} = W_B + W_P$ (solid lines) and radar reflectivity (shaded at 5, 15, 25, 35, and 45 dBZ), (d) $W_{BPL} = W_B + W_P + W_L$, (e) the Coriolis contribution plus numerical diffusion (W_{CD}), and (f) the net vertical acceleration (dW/dt).

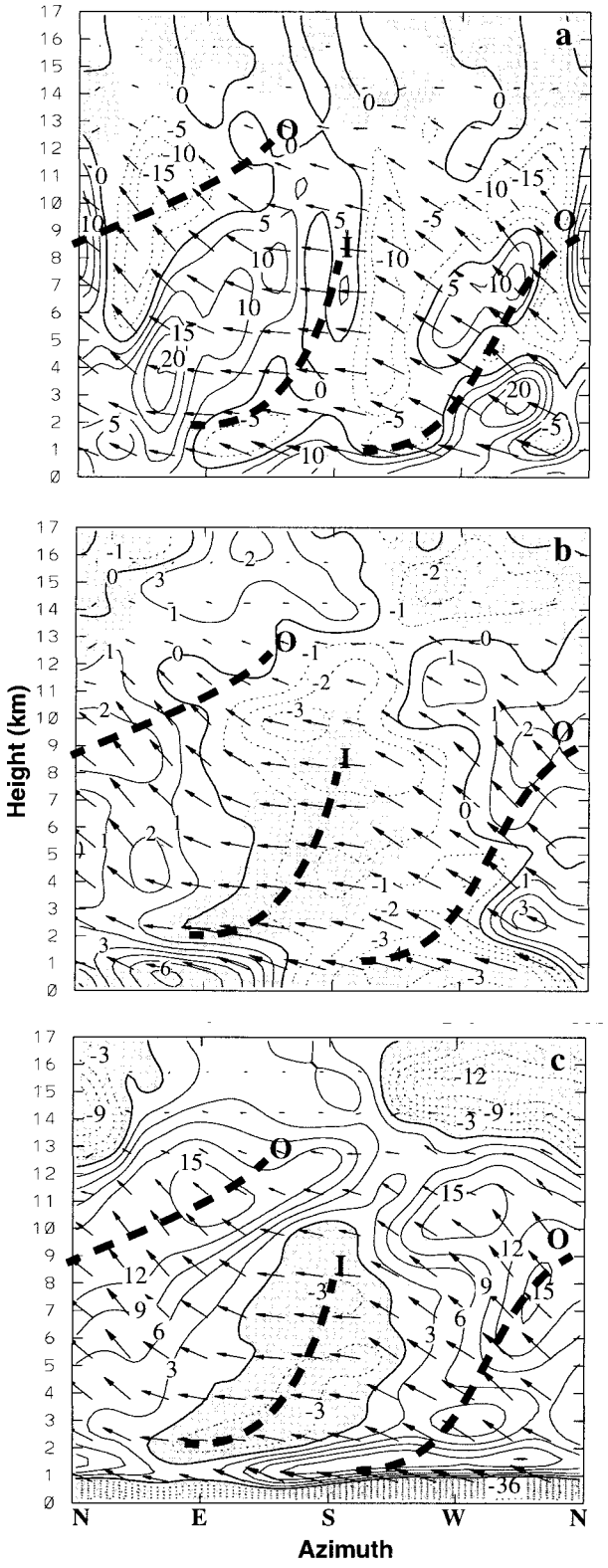

FIG. 4. Azimuth–height cross sections of (a) the vertical acceleration (dW/dt) at intervals of 5 m s^{-1} h^{-1} with the downdrafts shaded, (b) the θ_e deviations at intervals of 1 K with the inflows shaded, and (c) the system-relative radial flow at intervals of 3 m s^{-1} with the inflows shaded, which are taken, after the temporal average, along a slanting surface in the eyewall (i.e., from R = 30 km at the surface to R = 70 km at z = 17 km). The θ_e deviations are obtained by subtracting the azimuthally averaged values at individual heights. Thick dashed lines denote the axes of incoming (I) and outgoing (O) air. Thin solid (dashed) lines are for positive (negative) values. In-plane wind vectors are superposed.

mesh domain at 5-min intervals from the 56–57-h integration, valid at 2000–2100 UTC 23 August 1992. During this period, the simulated Andrew reaches a maximum surface wind of 68 m s^{-1} and a minimum surface central pressure of 935 hPa (see Fig. 2 in Part I). Each budget term, rather than each state variable, is first transformed from the model coordinates to the cylindrical coordinates with the minimum surface pressure of the storm at the origin. For most results presented herein, the terms are then averaged azimuthally (for each 5-min dataset) and temporally over the 1-h period. The details for performing the azimuthal average are given in Part II. Evidently, the above procedures could only introduce small interpolation errors that would not have a significant impact on the accuracy of budget calculations.

For ease of reference in subsequent discussions, we display in Fig. 2 the radius–height cross sections of the temporally and azimuthally averaged vertical motion (W), tangential (V) winds, absolute angular momentum [defined as AAM = $r(V + fr/2)$], and equivalent potential temperature (θ_e). In general, the flow structures are very similar, albeit slightly stronger in intensity due to the different temporal averaging, to those given in Fig. 3 of Part II. The eyewall is characterized by intense slantwise upward motion (UP) fed by an inflow within the maritime boundary layer (MBL). At the top of the eyewall, some air mass returns to the eye and descends all the way to the MBL along a narrow zone (DN) at the inner edge of the eyewall (Fig. 2a). Weak descent dominates the eye region. The mean axisymmetric tangential motion depicts a ring of intense flow with a maximum speed of V_{max} = 75 m s^{-1} at a radius of 30 km and an altitude of 800 m (Fig. 2b). The axis of the RMW lies outside the UP and slopes outward to a height of 10 km. Surface friction causes extremely large vertical shears in the MBL, especially in the region of the eyewall.

The magnitude of the mean AAM *decreases downstream* in the MBL inflow, but *increases downstream* in the top outflow layer (Fig. 2c). The AAM field shows large vertical gradients in both the inflow and outflow layers. The eyewall consists of dense sloping AAM surfaces that flatten out in the upper outflow layer. The updrafts follow closely constant AAM surfaces due to the intense baroclinicity across the eyewall (Shapiro and Willoughby 1982). In the saturated eyewall, the AAM surfaces are nearly parallel to the equivalent potential temperature θ_e surfaces, suggesting *the presence of a*

state of conditional symmetric neutrality (Emanuel 1986). However, strong potential instability is evident in the environment of the hurricane.

3. Vertical momentum budget

Figure 3 depicts all the budget terms in Eq. (2). The largest terms are the vertical PGF (W_P, Fig. 3a), local buoyancy (W_B, Fig. 3b), and water loading (W_L, not shown). Our choice of the running-average basic state leads to a small local buoyancy, which is of the same order of magnitude as W_P and W_L. It is important to note that W_P, calculated from the perturbation pressure p_1' (Fig. 1b), is positive in the eyewall and its outer precipitation regions. However, it is negative in the regions of slantwise penetrative downdraft (DN) and the eye below the peak warm-core level. By comparison, W_B shows a similar structure but is opposite in sign to W_P. The local buoyancy is predominantly positive in the eye below an altitude of 7.5 km but *predominantly negative in the eyewall* (Fig. 3b). The implication is that W_P tends to force relatively ''colder'' air to ascend in the eyewall and ''warmer'' air to descend in the eye. The ascending parcels in the eyewall are therefore negatively buoyant. A decomposition of W_B into its thermal (W_{BTV}) and dynamic (W_{BDP}) buoyancy indicates that W_{BTV} (shaded region in Fig. 3b) is indeed positive in the eyewall but it is overcompensated by the negative dynamic buoyancy (W_{BDP}). The local thermal buoyancy is very weak in the eyewall because ascending parcels are only slightly positively buoyant with respect to its outer region but negatively buoyant with respect to its inner region.

The sum of W_B and W_P ($=W_{\mathrm{BP}}$) is given in Fig. 3c, which shows that the vertical PGF almost completely cancels the local buoyancy force in the eye. However, a large positive residue, caused by the strong W_P, occurs in the eyewall and the outer precipitation region. The maximum in W_{BP} exceeds 110 m s^{-1} h^{-1} and is of the same order as W_P and W_B. The distribution of W_{BP} bears similarity to the simulated radar reflectivity (shaded in Fig. 3c), suggesting that water loading may play an important role in determining the net vertical acceleration in the eyewall. Indeed, Fig. 3d suggests that $W_L \sim -W_{\mathrm{BP}}$ because W_{BPL} ($=W_B + W_P + W_L = W_{\mathrm{BP}} + W_L$) is relatively small. This result indicates a quasi-balance between the net buoyancy ($W_B + W_L$) and W_P and implies that *the hydrostatic balance, traditionally used to estimate the surface pressure of hurricanes, is not valid in the eyewall unless the effect of water loading is included.*

The two remaining forces affecting the vertical acceleration are the Coriolis force (W_C) and numerical diffusion (W_D). The force W_C is related to the zonal component of the horizontal flow. At levels where the flow is mainly radial and directed outward, upward acceleration (deceleration) appears to the east (west) of the storm center. At levels where the flow is mainly tangential, upward acceleration (deceleration) is located to the south (north) of the center of the storm. Therefore, at the level for $V_{\max}$, a couplet of positive–negative acceleration centers would appear across the eye. For a wind speed of 50 m s^{-1} at a latitude of 25°N, W_C amounts to about 24 m s^{-1} h^{-1}, or approximately ¼ of the magnitude of water loading near the RMW. Thus, this component of the Coriolis force, omitted in hydrostatic models, should be included in estimating the vertical acceleration in the eyewall. However, the azimuthal averaged W_C is quite small and it vanishes completely if the storm is axisymmetric.

The vertical and horizontal numerical diffusion W_D is designed to damp vertical acceleration/deceleration. It gives rise to a wavelike structure similar to the vertical motion (cf. Figs. 3e and 2a). However, its magnitude is small when compared to other terms in Eq. (2) and can be ignored in the discussion of the budgets.

The total vertical acceleration (dW/dt) is positive in the eyewall. Its magnitude decreases upward and its sign changes beyond the level of maximum updraft (cf. Figs. 3f and 2a). The peak vertical acceleration in the vicinity of $V_{\max}$ (cf. Figs. 3a,f and 2b) is associated with W_P, indicating the importance of PGF in lifting convection in the eyewall. Maximum deceleration occurs just below the upper divergent outflow layer due mainly to the negative buoyancy (cf. Figs. 3b,f). At the melting level (i.e., near 5 km) outside the eyewall, the total acceleration is also downward and coincides with the location of enhanced downdrafts. Note a deep but narrow zone of negative acceleration down to 800 m located between the inner portion of the updrafts in the eyewall and the outer portion of the downdrafts in the eye (i.e., outside the line DN). This zone is highly divergent (see Fig. 3g in Part II) and represents upward deceleration (downward acceleration) of the parcels in the updrafts (downdrafts). As will be shown in Fig. 4, the zone is substantially influenced by the upper return inflow and is driven by cooling from sublimation/evaporation in the inflowing air. Similarly, the acceleration in the inner portion of the downdrafts is attributable to downward deceleration of air parcels from the positive buoyancy in the eye (cf. Figs. 3f and 3b). Further inward toward the center and away from the intense downdraft, a weak but organized wavelike acceleration pattern can be detected. The pattern is the result of the residue between W_P and W_B and has a magnitude of about ± 1 m s^{-1} h^{-1}. It provides some evidence for unbalanced forces that generate inertial–gravity waves in the eye discussed in Part II.

A better understanding of the acceleration/deceleration structures could be obtained from the *slanting* azimuth–height cross sections of the total vertical acceleration (Fig. 4a), deviation θ_e (Fig. 4b), and radial flows (Fig. 4c) in the sloping eyewall. Note the increase in horizontal length scale with height that has the ratio of 7:3 between the top and bottom boundaries due to the rectangular mapping of a trapezoidal surface associated

with the slanting cross section. Note also that the upper portion of the cross sections lies within the eye and are marked by weak descending and tangential flows (Figs. 2a,b). On average, the vertical acceleration is similar to its axisymmetric structures (i.e., negative above and positive below). However, the temporally averaged azimuthal distribution is highly asymmetric and well organized, with values ranging between ± 20 m s^{-1} h^{-1}. Of importance is that the wavenumber-1 vertical acceleration[1] tilts downshear and it is correlated, with some phase lag, to the distribution of radial inflow/outflow (cf. Figs. 4a,c) due to the pronounced thermal and moisture gradients across the eyewall.[2] For example, Fig. 4b shows that the incoming dry and cold (or lower θ_e) environmental air tends to cause sublimative/evaporative cooling in the eyewall, especially in the upper layers, thereby inducing downdrafts or suppressing updrafts in the vicinity of the inflow (I) axis. In contrast, most of the outgoing air is moist and warm (or higher θ_e), so it facilitates the development of updrafts along the outflow (O) axis. All this can be clearly seen from the correlation between in-plane flow vectors and radial flows given in Fig. 4c. Again, more intense updrafts appear in the outflow region (e.g., in the northern semicircle).

Despite the well-organized vertical acceleration/deceleration structures in the inner-core region, the net accelerations/decelerations (± 20 m s^{-1} h^{-1}) are only about 0.07% of the gravitational acceleration or at least one order of magnitude smaller than any of the three forces on the rhs of Eq. (2), that is, W_P, W_B, and W_L. This result implies that *nonhydrostatic effects are small in hurricanes* and that hydrostatic primitive equations may be used to simulate them at the grid size down to 6 km, provided that realistic cloud microphysics processes and water loading are incorporated. The small nonhydrostatic effect could be attributed to the fact that the vertical forces are in approximate balance so that vertical motion in the eyewall is much weaker than in other severe storms, such as tornadic and midlatitude thunderstorms (Jorgenson et al. 1985).

The Lagrangian tendency provides a measure of force balance associated with a parcel. To obtain local changes in the vertical motion, we need to understand advective contributions. Figure 5a shows that horizontal advection by the low-level inflow reduces (increases) the updraft intensity in the outer (inner) portion of the eyewall, thereby advecting the updraft axis inward—a sign of eyewall contraction. In contrast, horizontal advection by the upper-level outflow increases (decreases) the updraft intensity in the outer (inner) portion of the eyewall, thus advecting the updraft axis outward and causing the outward sloping of the eyewall. On the other hand, the slantwise advection in the midtroposphere by the sloping flow tends to weaken (enhance) the updraft below (above) the updraft axis. Note that the total advection and net Lagrangian tendency (cf. Figs. 3f and 5a) show similar patterns with opposite signs. Their difference, representing the local tendency of vertical motion (Fig. 5b), is one order of magnitude smaller than each individual term. This result indicates that (i) any imbalance generated by the vertical PGF (W_P), the local buoyancy (W_B), and water loading (W_L) could be rapidly advected away by the intense tangential winds; and (ii) on average

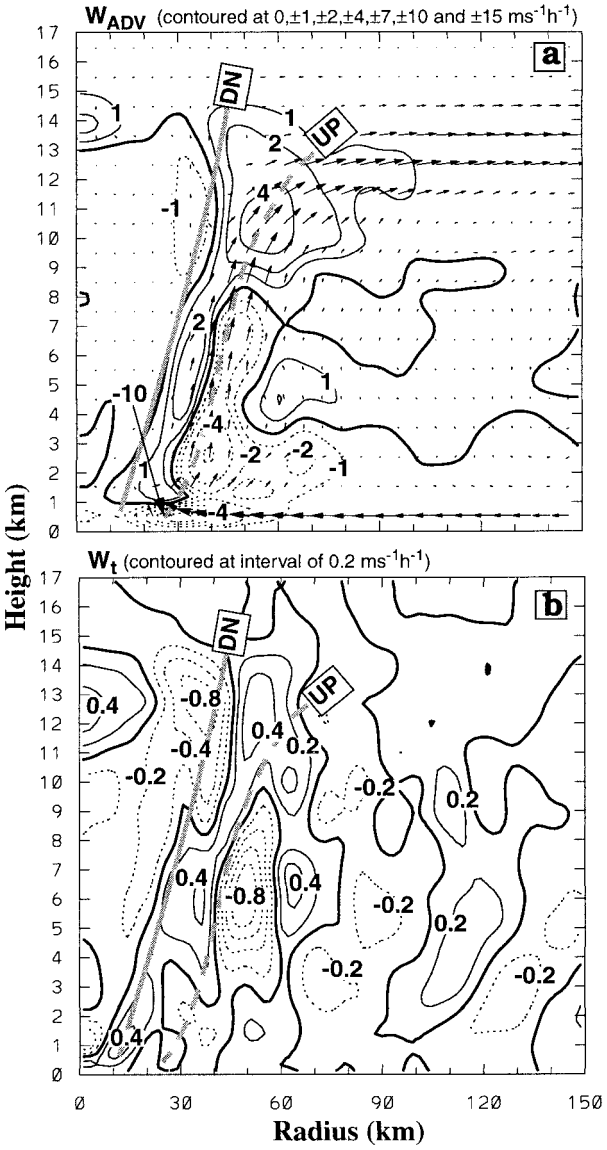

FIG. 5. As in Fig. 1 but for (a) total advection (W_{ADV}) and (b) local tendency (W_l) in the vertical momentum equation.

[1] The instanteous fields of most state variables appear in a wavenumber-2 structure and propagate downshear cyclonically; they will be discussed in a forthcoming article in association with unbalanced flows. They have been aliased into the wavenumber-1 structure herein due to the use of temporal averaging.

[2] As shown in Part I, the maximum radial thermal gradient is as large as 16 K (80 km)$^{-1}$ from the center of the eye to the outer edge of the eyewall.

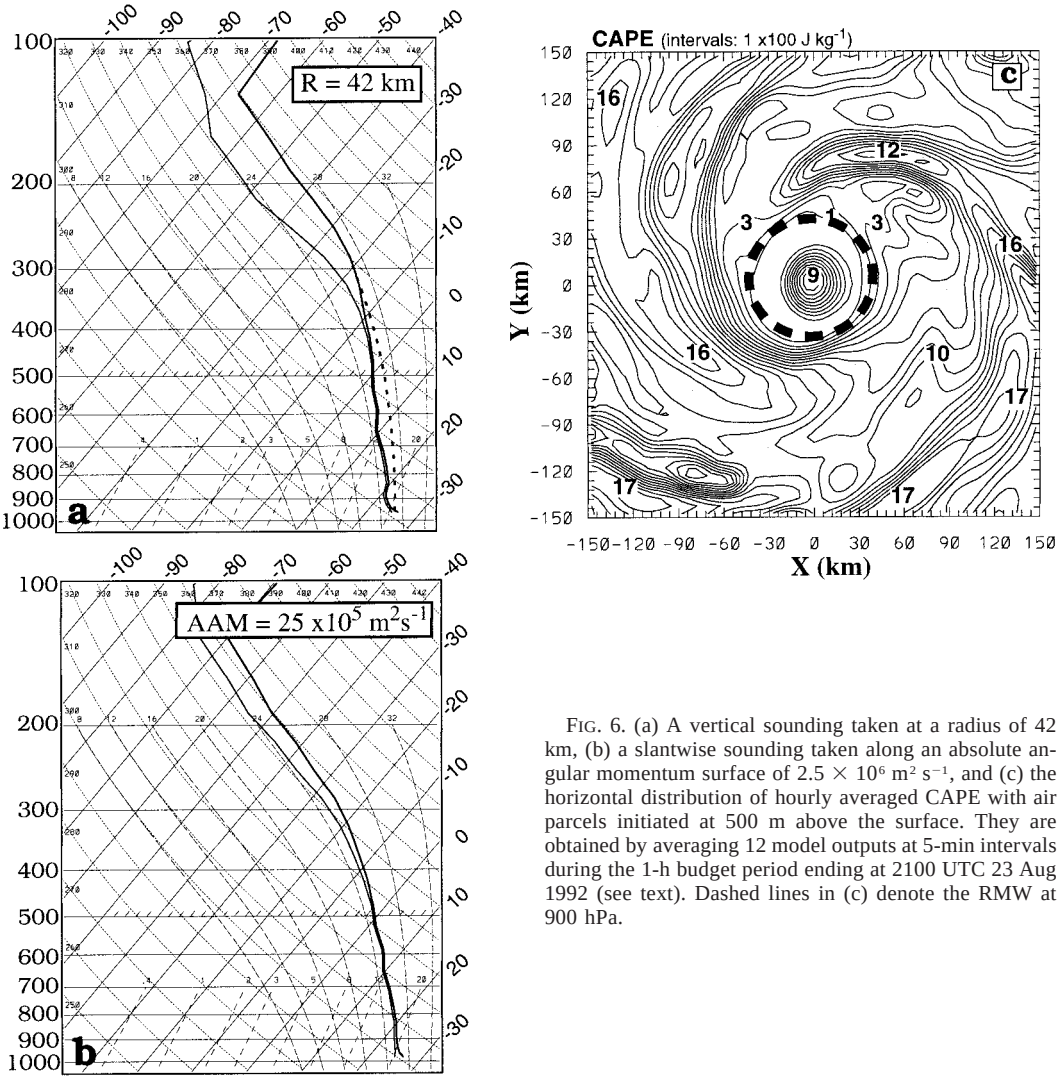

FIG. 6. (a) A vertical sounding taken at a radius of 42 km, (b) a slantwise sounding taken along an absolute angular momentum surface of 2.5×10^6 m^2 s^{-1}, and (c) the horizontal distribution of hourly averaged CAPE with air parcels initiated at 500 m above the surface. They are obtained by averaging 12 model outputs at 5-min intervals during the 1-h budget period ending at 2100 UTC 23 Aug 1992 (see text). Dashed lines in (c) denote the RMW at 900 hPa.

the eyewall and its surrounding vertical motion tend to evolve slowly despite the rapid deepening in central pressure during the intensifying stage (Smith 1980; Emanuel 1997).

In spite of the small net local tendency (about ± 0.8 m s^{-1} h^{-1}), there is clearly a sign of intensification (weakening) of the updraft in its inner (outer) portion (Fig. 5b). Thus, the eyewall tends to shrink in radius during the intensifying stage, consistent with the contraction shown in Part II. Meanwhile, the downdraft, initiated in the upper levels at the inner edge of the eyewall, will strengthen and contract in radius (cf. Figs. 5b and 2a). As expected, the local change in vertical motion in the eye is small, in agreement with the simulated weak subsidence. The positive tendency between 11- and 14-km altitude could be considered as part of the inertial–gravity wave propagation in the eye. Outward from the eyewall beyond a radius of 80 km, the positive local tendency that favors updraft development is associated with the outer spiral rainbands.

We finally address a question raised in the introduction concerning the thermodynamic energy associated with convection in the eyewall. An azimuthally averaged sounding taken in the eyewall (Fig. 6a) exhibits near-saturated conditions in the eyewall and drier air aloft in the eye. Little CAPE or even negative buoyancy is present for parcels released above the MBL (i.e., above 900 hPa or 50 hPa above the surface). The distribution of CAPE in the horizontal (Fig. 6c) indicates considerable CAPE in the storm's environment, consistent with the large potential instability in the ambiance of the hurricane (Fig. 2c). However, little CAPE is present in the eyewall except at its outer edge. Of course, this result does not imply that the environmental high-θ_e air has little impact on convection in the eyewall. In fact, the eyewall convection is driven by the high-θ_e air

in the bottom inflow layer, but its potential instability decreases as the air moves inward due to midtropospheric warming/moistening from prior convection (see Fig. 2c). As will be demonstrated in the next section, this high-θ_e air ascends along a constant slantwise θ_e surface in the eyewall (with little potential instability or CAPE) as a result of dynamic lifting. By comparison, Fig. 6b depicts an azimuthally averaged sounding along an absolute angular momentum surface at the center of the eyewall. Positive SCAPE, consistent with the average magnitude of slantwise updrafts of 2 m s^{-1}, is indicated. Thus, the results of our simulation suggest that the eyewall convection occurs under conditionally stable but slantwise unstable to neutral conditions (Fig. 2c), in agreement with previous theoretical hypotheses (e.g., Emanuel 1986).

4. Dynamically induced vertical motion

The vertical momentum budget in the preceding section shows clearly the relative importance of individual forces in the generation of vertical acceleration. However, the perturbation PGF contains both dynamic and buoyancy effects. To unravel the contributions from the dynamics and buoyancy, we rewrite Eq. (2) in a manner following Rotunno and Klemp (1982) as

$$\frac{dW}{dt} = \left(W_{\rm CD} - \frac{1}{\rho}\frac{\partial P_d}{\partial z}\right) + \left(b - \frac{1}{\rho}\frac{\partial P_b}{\partial z}\right), \qquad (4)$$

where

$$b = g\left(\frac{\overline{\rho}}{\rho}\frac{T_v'}{T_v} - \frac{P'}{p}\right) - g(q_c + q_r + q_i + q_s + q_g), \qquad (5)$$

$$W_{\rm CD} = 2\Omega u_m \cos\phi + D_w, \qquad (6)$$

and P_d and P_b are the dynamic and buoyancy perturbation pressures, respectively. The variable P' ($=P_d + P_b$) is the total perturbation pressure from the basic state.

Equation (4) states that the vertical momentum acceleration is determined by the net dynamic force ($W_{\rm ND} = W_{\rm CD} + {\rm PGF}_d$) and the net buoyancy force ($W_{\rm NB} = b + {\rm PGF}_b$). To calculate ${\rm PGF}_d$ and ${\rm PGF}_b$, we obtain P_d and P_b by inverting a 3D pressure equation. Because of the restriction of the solver in solving the pressure equation, we adopted the basic state $\overline{p}(z, t)$ in our inversion. The derivation of the pressure equation, together with the definition of the basic state and the boundary conditions for inversion, are given in the appendix. Obviously, if the pressure obtained from the inversion is accurate, the azimuthally averaged P' should be very close to p_2' introduced in section 2.

Figures 7a,b present cross sections of the azimuthally averaged P_b and P_d, respectively, while Fig. 7c depicts the difference field between the azimuthally averaged P' and p_2' (given in Fig. 1a). Although the error in the inverted P' is $<1\%$ and amounts to only 0.1 to -0.2 hPa in the eye, large errors can result in computing the vertical acceleration because the magnitude of which is one to two orders smaller than the individual terms on the rhs of Eq. (2) (see Fig. 3). Hence, it is not meaningful to discuss the residues between $W_{\rm ND}$ and $W_{\rm NB}$.

Figures 7d and 7e show quite different structures between the buoyancy and dynamic sources (see the appendix for definition) in producing the associated perturbation pressures (i.e., P_b and P_d). For example, the buoyancy source F_b is mostly negative, and it appears in a deep layer up to 14 km and tilts with height to a radius of >80 km in the upper outflow layer (Fig. 7d). In contrast, the dynamic source F_d is nearly all positive and concentrated in the lowest few kilometers (Fig. 7e). Since the momentum advection is maximized at the RMW and minimized at the eye's center, the dynamic source is more concentrated in the region in between and its magnitude decreases rapidly upward. The localized dynamic source at 1-km altitude is associated with the vertical advection of tangential winds. This low-level positive dynamic source does not seem to contribute significantly to the inverted P_d due partly to its shallowness and partly to the compensation by the negative source below. Furthermore, the Laplacian operator tends to smear out any small-scale influences.

The buoyancy-induced P_b decreases rapidly with height with a reversal of the sign of the horizontal gradients at 7 km where the peak warm core is located. However, the dynamically induced P_d exhibits a ''near barotropic'' structure in the vertical with only a slight tilt in the eye (cf. Figs. 7a,b). It is important to note that *a large portion of the buoyancy perturbation pressure is produced by the warming associated with moist-adiabatic ascent in the eyewall and the subsidence warming in the eye.* It accounts for more than 55 hPa of the pressure drop at the surface, or roughly 70% of the total pressure deficit (cf. Figs. 7a and 1a). By comparison, the dynamically induced P_d is about -22 to -25 hpa at the eye's center. Such a dynamically induced central pressure drop finds analogy in a rotating cylindrical vessel filled with water. That is, the faster the rotation, the steeper is the parabolic free surface, and the lower the pressure at the bottom surface.

In spite of the near-barotropic structure, ${\rm PGF}_d$ points downward (negative) within the radius of the tilted updraft core but upward (positive) outside (Fig. 8a). Its value becomes negligible beyond $R = 80$ km. Since the azimuthally averaged $W_{\rm CD}$ is small (see Fig. 3e), the net dynamic force $W_{\rm ND}$ is nearly the same as ${\rm PGF}_d$ except in the MBL. Clearly, the downward ${\rm PGF}_d$ tends to suppress the upward convective current in the inner portion of the eyewall and forces it to tilt outward. In the outer portion of the eyewall, the upward (or positive) ${\rm PGF}_d$ helps to lift low-level high-θ_e air to the condensation level to facilitate the development of convection. This result is in qualitative agreement with that obtained in section 3. Note that both the upward and downward ${\rm PGF}_d$ are peaked in the midtroposphere (7–8 km), and the peak downward ${\rm PGF}_d$ is centered at a radius of 12

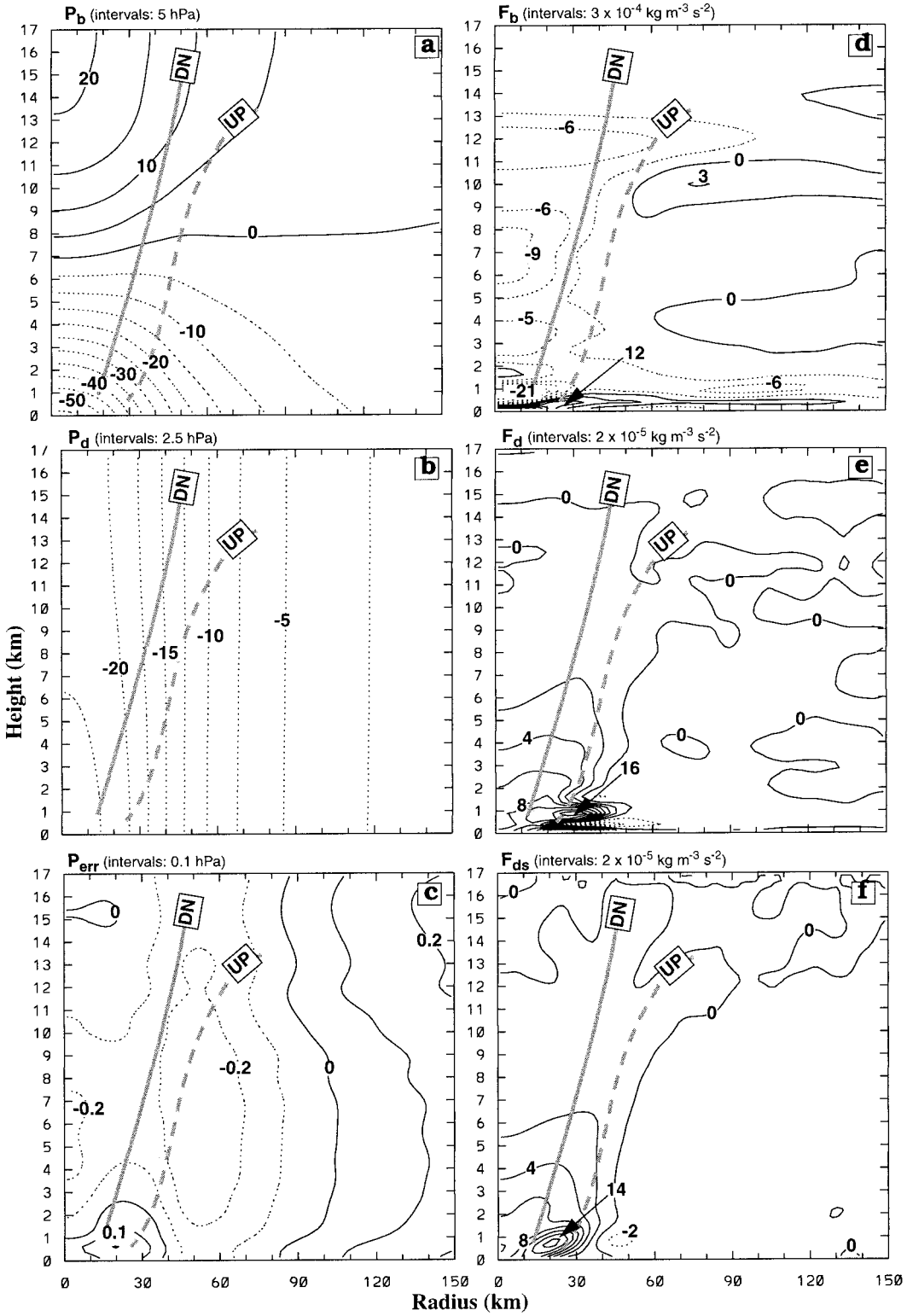

FIG. 7. As in Fig. 1 but for (a) the buoyancy-induced pressure perturbation (P_b) at intervals of 5 hPa, (b) the dynamically induced pressure perturbation (P_d) at intervals of 2.5 hPa, (c) the difference field between the perturbation pressure p'_2 shown in Fig. 1a and the azimuthally averaged inverted P' ($=P_d + P_b$), (d) the buoyancy source (F_b) for P_b, (e) the dynamic source (F_d) for P_d, and (f) the approximated dynamic source [i.e., $F_{ds} = (\rho/r)(\partial V^2/\partial r,)$ which is the first term on the rhs of Eq. (9b)].

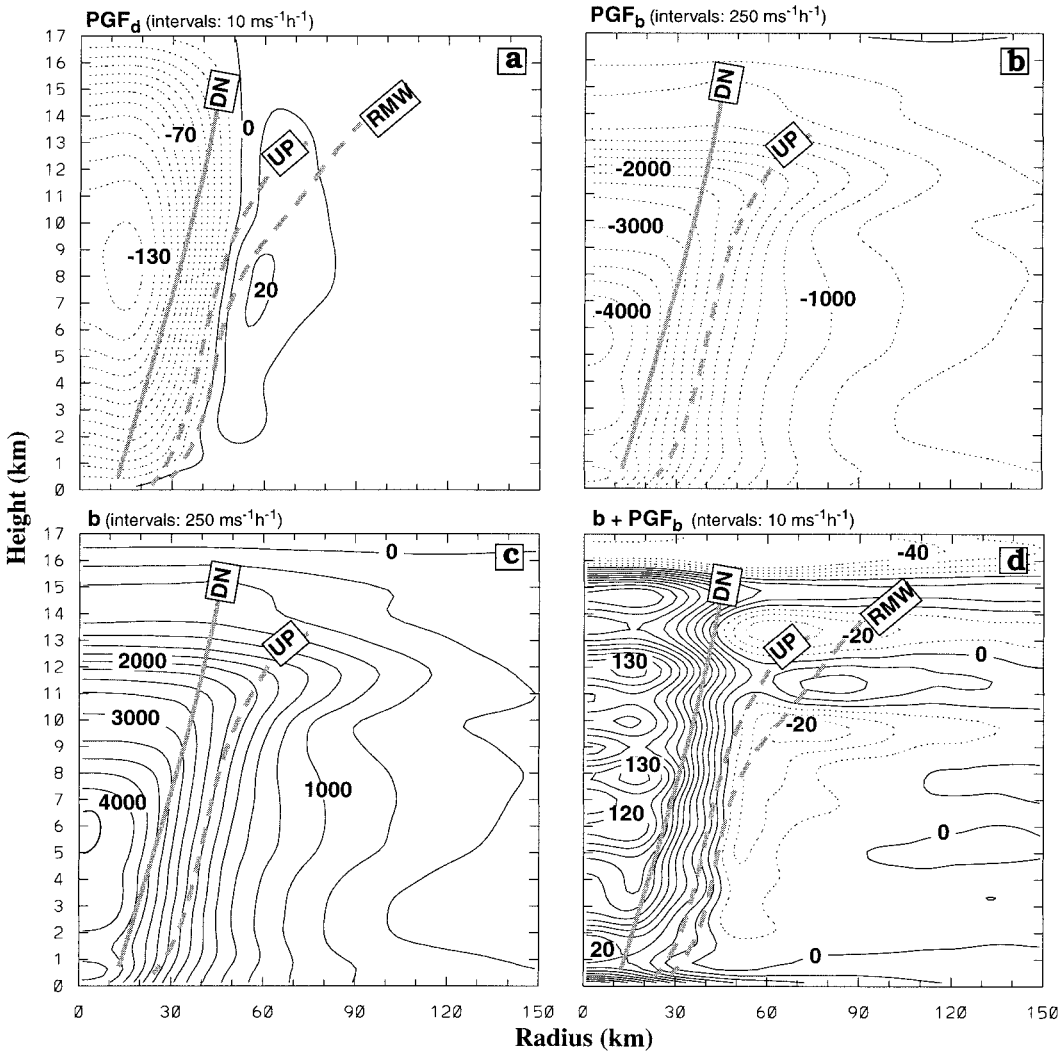

FIG. 8. As in Fig. 1 but for (a) the dynamically induced PGF$_d$, (b) the buoyancy-induced PGF$_b$, (c) the buoyancy force (i.e., b), and (d) the net buoyancy force (i.e., W_{NB} = PGF$_b$ + b).

km. This horizontal displacement of the peak downward PGF$_d$ from the central axis appears to result from the azimuthally asymmetric distribution of tangential winds at the RMW [cf. Fig. 7 in Zhang et al. (1999) and Fig. 9 herein].

The large buoyancy-induced P_b results in extremely intense downward PGF$_b$, more than one order of magnitude larger than PGF$_d$, particularly in the eye (cf. Figs. 7a and 8b). The PGF$_b$ is similar in structure and magnitude but opposite in sign to the buoyancy (cf. Figs. 8b,c). Thus, the net buoyancy force W_{NB} (=b + PGF$_b$; Fig. 8d) is a small difference between two large terms, but it is responsible for various fluctuations in the vertical. On average, W_{NB} and the dynamically induced PGF$_d$ have similar magnitude but they oppose each other (cf. Figs. 8a,d). Since it is meaningless to examine the residues between W_{NB} and W_{ND}, we may state that *the dynamically induced PGF$_d$ must be larger than, but be in close balance with the net buoyancy force W_{NB}, to maintain the general descent over a deep layer in the eye during the intensifying stage. The same should also be true for the lower-tropospheric ascent in the outer portion of the eyewall.* The inner portion of the eyewall may be viewed as a transition zone where air parcels in both UP and DN decelerate vertically. This result further reveals that positive buoyancy is not necessary for continued deepening of the hurricane as long as high-θ_e air is available in the vicinity of the eyewall.

Figure 9 compares the horizontal distributions of net dynamic force W_{ND} and net buoyancy force W_{NB} at three selected levels. In general, W_{ND} overcompensates W_{NB} in the eye but the cores of W_{ND} and W_{NB} do not quite coincide with the eye center. A deep layer of strong positive W_{ND} appears in the north semicircle and southwest quadrant of the storm, formed partly from the positive PGF associated with the intense low-tropospheric

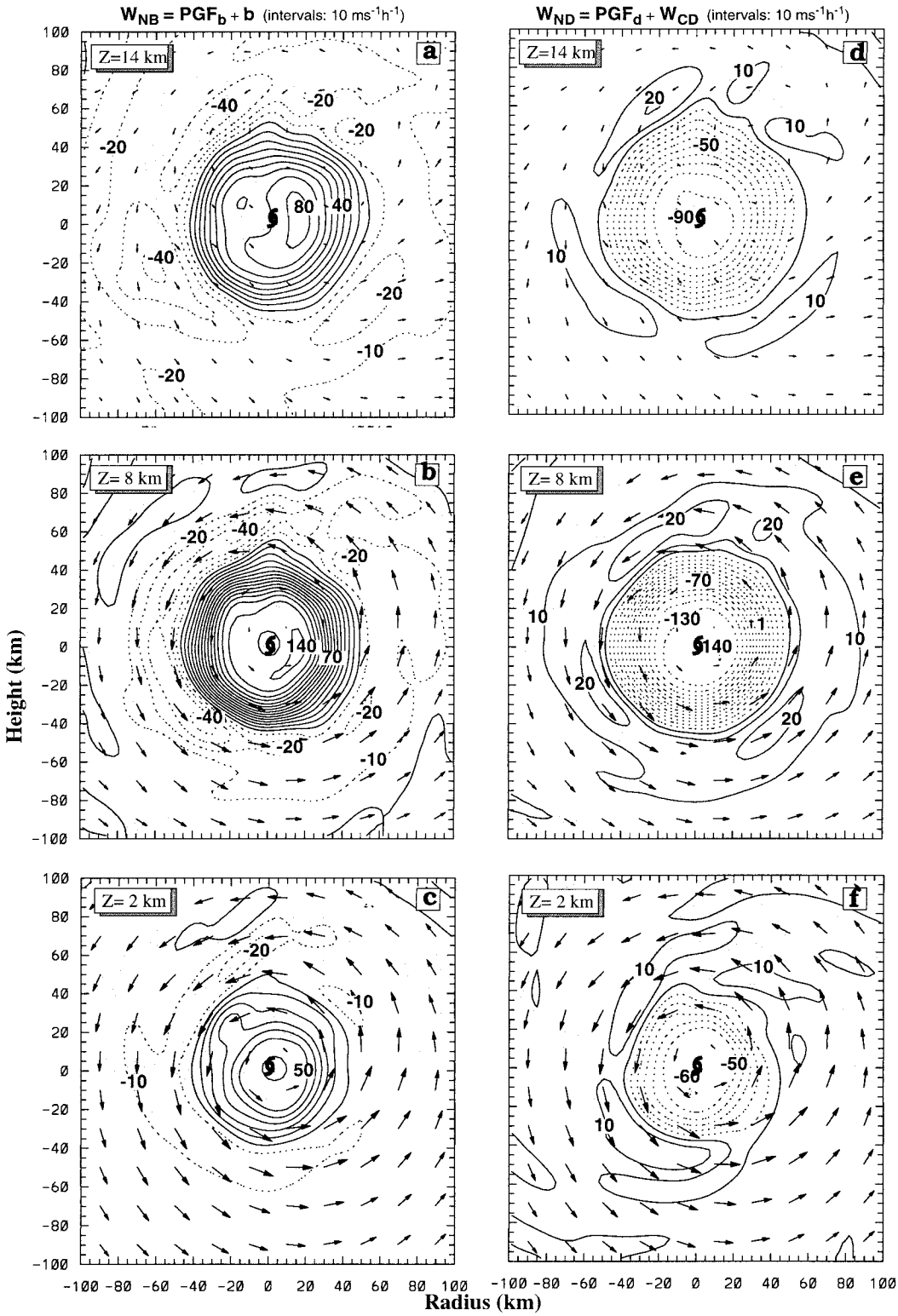

FIG. 9. Horizontal distributions of (a)–(c) the net buoyancy force (i.e., $W_{NB} = PGF_b + b$) and (d)–(f) the net dynamic force (i.e., $W_{ND} = PGF_d + W_{CD}$) at intervals of 10 m s^{-1} h^{-1} at the given heights (i.e., z = 14, 8, and 2 km) over a subdomain of the 6-km resolution mesh. They are obtained by averaging 12 model outputs at 5-min intervals during the 1-h budget period ending at 2100 UTC 23 Aug 1992 (see text). Shadings denote the system-relative radial inflow at these levels.

tangential winds in these regions, offset somewhat by the negative PGF associated with the Coriolis force. It is important to note that the upward W_{ND} is distributed in the system-relative radial inflow region, in the shape of spiral rainbands in the north semicircle (Fig. 9f). Obviously, this upward W_{ND} contributes to the lifting of high-θ_e air to facilitate convective development in the inflow region of the eyewall. This result appears to have some implications with respect to the strategy of adaptive observations to locate more intense convective developments if such inflow regions could be identified in an operational setting.

To further understand the roles of the dynamic force W_{ND} in inducing vertical motion, we examine the dynamic sources in Eq. (A2). A scale analysis shows that PGF_d is dominated by the divergence of horizontal momentum advection, namely,

$$-\nabla\cdot(\rho\mathbf{V}\cdot\nabla\mathbf{V}) = -\rho\left[\nabla_h^2\frac{\mathbf{V}_h^2}{2} - \nabla_h\cdot(\mathbf{V}_h\times\zeta\mathbf{k})\right] + R \quad \text{and} \tag{7}$$

$$R = -\rho\nabla\cdot\left(W\frac{\partial\mathbf{V}}{\partial z} + \mathbf{V}_h\cdot\nabla W\right) - (\mathbf{V}\cdot\nabla\mathbf{V})\cdot\nabla\rho, \tag{8}$$

where the subscript h denotes the horizontal component and ζ is the vertical component of vorticity. In cylindrical coordinates, and after performing an azimuthal average, Eq. (7) can be written as

$$\langle\nabla\cdot(\rho\mathbf{V}\cdot\nabla\mathbf{V})\rangle = -\frac{\rho}{r}\frac{\partial}{\partial r}\left[r\frac{\partial(\mathbf{V}_h^2/2)}{\partial r}\right] + \frac{\rho}{r}\frac{\partial}{\partial r}\left[\mathbf{V}_h\frac{\partial(r\mathbf{V}_h)}{\partial r}\right] + R \tag{9a}$$

$$\approx \frac{\rho}{r}\frac{\partial V^2}{\partial r} + R, \tag{9b}$$

where angle brackets $\langle\cdot\rangle$ denote the azimuthal average operator and the contribution of the radial flows has been neglected in obtaining the final approximation. Equation (9b) is essentially the cyclostrophic approximation, and it states that the azimuthally averaged dynamic source is dominated by the radial shear of V^2 weighted by the radial distance, which is evident by comparing the dynamic sources as computed from F_d and $(\rho/r)(\partial V^2/\partial r)$ (cf. Figs. 7e and 7f). Our result therefore differs from that of Rotunno and Klemp (1982) and Klemp and Rotunno (1983), where the important dynamic source in thunderstorm rotation and movement is the tilting of horizontal vorticity (associated with vertical wind shear) by nonuniform vertical motion. In our case, it is the low-level intense tangential winds at some distance from the circulation center, not their negative vertical shear, that is responsible for the general subsidence warming in the eye. It appears that Eq. (9b) could also be applied to other rotating weather systems, such as the decending motion in the core of tornadoes (R. Wakimoto 1999, personal communication).

To substantiate the above analysis, Fig. 10 shows the azimuthally averaged PGF induced by the Laplacian of horizontal kinetic energy, the radial gradient of ''azimuthal vorticity advection,'' and the residual source R on the rhs of Eq. (7) [which are equivalent to those in Eq. (9a)]. One can see the opposing (or cancellation) effect between the first two components from their opposite signs. Obviously, the radial shear of the tangential winds dominates the dynamics of the simulated hurricane (Fig. 10b). Since both V and ζ are intense at the RMW, the more compact the storm is, the stronger is the upward (downward) PGF_d at the outer portion of the eyewall (in the eye). *The net dynamic force is associated mostly with the radial gradient of V^2 weighted by radius*, similar to what is depicted in Fig. 8a. The residual source, dominated by the divergence of vertical advection of horizontal winds or the tilting of horizontal vorticity, indicates a deep layer of upward PGF_d within the RMW and it corresponds well to the strong vertical shear in the region (cf. Figs. 2b and 8a). This result is qualitatively in agreement with that of Rotunno and Klemp (1982) in their thunderstorm studies. However, the positive contribution of vertical shear is clearly small compared to the large negative PGF_d generated by the radial shear within the RMW (cf. Figs. 10b,c).

Based on the above results, we propose a different theoretical explanation for the relationship among the subsidence warming in the eye, and the rotation and vertical shear in the eyewall. Specifically, as tropical cyclogenesis occurs, the lower-level tangential winds must intensify in accordance with gradient wind balance. The radial shear of the tangential winds in turn increases and induces a deep layer of downward PGF_d. If this downward dynamic force could gradually overcome the positive buoyancy, the air near the center of the vortex circulation will be forced to subside, thereby leading to warming and drying, and the formation of a hurricane eye and the further deepening of the storm. As a result of the middle- to upper-level warming, the tangential winds in the eyewall must decrease with height, as dictated by the thermal wind relation. Thus, *the negative vertical shear in the eyewall is caused by the forced subsidence warming, rather than the other way around as suggested by previous studies.* Our different explanation is based on the inverted PGF_d, which shows that it is the low-level radial shear, rather than the vertical shear, of the tangential winds that drives the general descent in the eye. Of course, the dynamically driven subsidence warming must occur at a rate to ensure near-hydrostatic balance in a stratified fluid. Moreover, in order for the net dynamic force to overcome the net buoyancy force, the eyewall convection must be able to transport sufficient angular momentum upward to intensify the rotation of the eyewall; this will be discussed in Part IV of this series of papers.

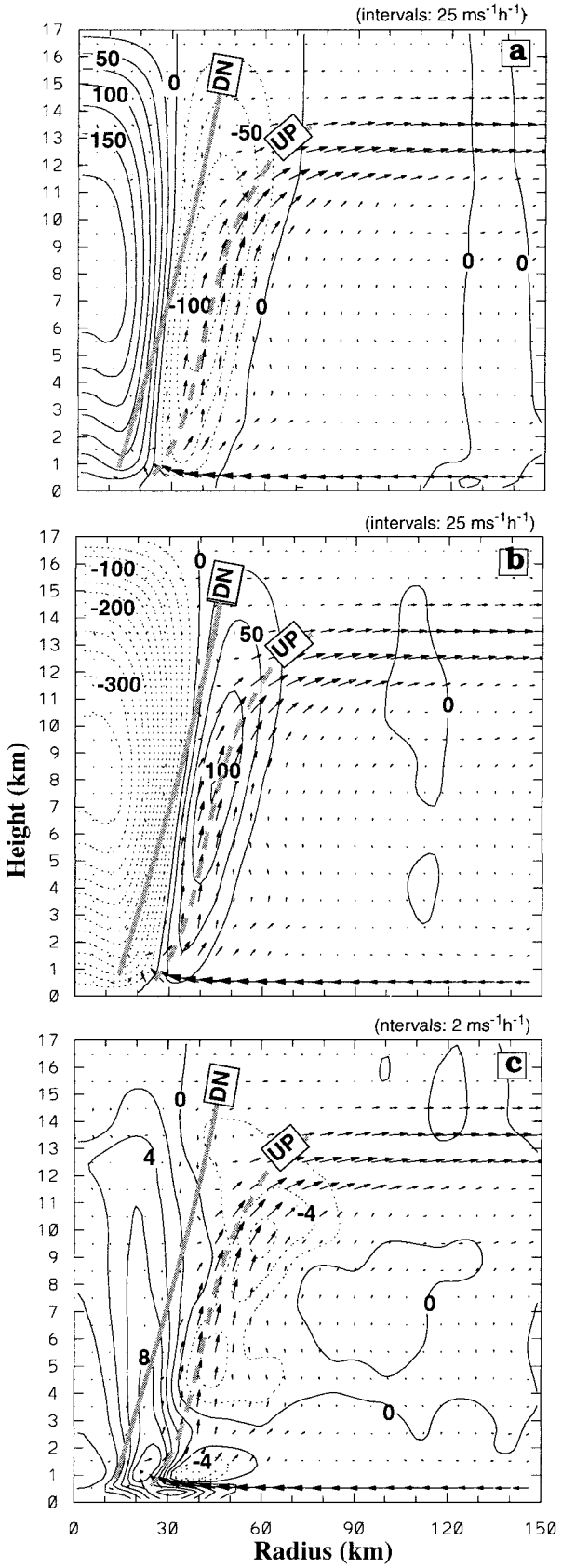

5. Summary and conclusions

In this study, we have examined the vertical force balance in the inner-core region using a high-resolution ($\Delta x = 6$ km), explicit simulation of Hurricane Andrew (1992). The vertical momentum budgets are first calculated directly from the output of a 1-h model integration at 5-min intervals, and then they are azimuthally and temporally averaged to reveal axisymmetric features. Asymmetries in the vertical structures as related to the primary circulations are also studied. Finally, the 3D perturbation pressures induced by the dynamic and buoyancy sources were obtained to gain insight into the processes for subsidence warming in the eye and the vertical lifting at the outer edge of the eyewall in the absence of positive buoyancy.

The vertical momentum budget shows that the vertical acceleration in the eyewall is a small difference among the three large terms, that is, positive perturbation PGF, negative buoyancy, and water loading. The result suggests that the water loading effects have to be included into the hydrostatic equation in estimating the surface pressure in precipitation regions. Hydrostatic models may be used to simulate hurricanes down to a grid size of 6 km, provided that some cloud microphysics processes and water loading are properly incorporated. The azimuthally averaged convection in the eyewall is found to be conditionally stable but slantwise unstable. Little positive CAPE is present despite considerable potential instability in the storm environment. It is the perturbation PGF that provides the necessary forcing for the upward acceleration of parcels in the lower portion of the eyewall. Nevertheless, the local rates of change in vertical motion are very small due to rapid advection in the eyewall.

It is found that the azimuthal distributions of vertical motion and acceleration, even after being temporally averaged, are highly asymmetric but well organized into a wavenumber-1 pattern. We emphasize that the asymmetric dynamics of vertical motion is closely related to the radial inflow/outflow structures in conjunction with the large thermal and moisture gradients from the eye to the outer edge of the eyewall. Specifically, in the central portion of the eyewall, the radially incoming cold and dry environmental air tends to cause sublimation and evaporative cooling, thus inducing downdrafts in the upper levels or suppressing updrafts below. However, the outgoing moist and warm air tends to assist the development of more intense updrafts in the eyewall.

Because the vertical PGF contains both the dynamic and buoyancy effects, the 3D perturbation pressures are inverted to determine the individual dynamic and buoyancy sources. The results show that a large portion of

←

FIG. 10. As in Fig. 1 but for the decomposed components of PGF associated with the term (a) $\rho\nabla_h^2(V_h^2/2)$, (b) $\rho\nabla_k \cdot (\mathbf{V}_h \times \zeta\mathbf{k})$, and (c) the residual [see Eq. (7) for definitions].

the perturbation pressure is produced by the warming associated with moist-adiabatic ascent in the eyewall and subsidence warming in the eye. The buoyancy-induced surface central pressure drop accounts for roughly 70% of the total deepening. Despite the large magnitude, the buoyancy-induced PGF is mostly offset by the buoyancy force itself, and their net effect is similar in magnitude but opposite in sign to the dynamically induced PGF. It is found that the net dynamic force (W_{ND}) points downward in the eye and accounts for the maintenance of the general descent in the eye. However, W_{ND} points upward in the outer portion of the eyewall, particularly in the north semicircle, and facilitates the lifting of high-θ_e air from the lower troposphere into the storm. This result suggests that positive CAPE is not necessary for continued deepening of hurricanes as long as high-θ_e air could be available in the MBL in the storms' environment.

More importantly, our study shows that it is the radial shear, rather than the vertical shear, of tangential winds that is responsible for the downward (upward) dynamic force in the eye (outer portion of the eyewall). Based on this finding, a different theoretical explanation is provided for the relationship among the subsidence warming in the eye, and the rotation and vertical shear in the eyewall. Specifically, as a positive radial shear is built up during the deepening stage, a deep layer of downward PGF_d could be induced in the inner-core region of a tropical storm. If this downward force could gradually overcome the net buoyancy as a result of faster rotation of the eyewall, it may force the air to subside, leading to warming and drying, the formation of an eye, and the further deepening of the storm. As a consequence of midlevel warming, the tangential winds must decrease with height, as dictated by the thermal wind relation. Thus, we may conclude that the negative vertical shear in the eyewall is caused by the forced subsidence warming, rather than the other way around as suggested by previous studies. It follows that the general weak descent in the eye occurs passively, in response to the intensity of low-level tangential winds.

Acknowledgments. We thank Bill Kuo and Y.-R. Guo at NCAR/MMM for providing the budget calculation codes, and Drs. Fred Baer and Ming Cai for their helpful discussions. This work was supported by NSF Grant ATM-9802391, NASA Grant NAG-57842, and ONR Grant N00014-96-1-0746. The computations were performed at the National Center for Atmospheric Research, which is sponsored by the National Science Foundation.

APPENDIX

Inversion of Three-Dimensional Perturbation Pressures

The three-dimensional Euler momentum equation in Cartesian coordinates can be written as

$$\rho\frac{\partial \mathbf{V}}{\partial t} = -\rho\mathbf{V}\cdot\nabla\mathbf{V} - \nabla P' + \rho b\mathbf{k} - 2\rho\Omega\times\mathbf{V} + \rho\mathbf{D}_v, \quad \text{(A1)}$$

where $\mathbf{V} = U\mathbf{i} + V\mathbf{j} + W\mathbf{k}$, ∇ is the three-dimensional gradient operator, P' is the perturbation pressure from the basic state $\overline{p}(z, t)$, $\mathbf{D}_v$ includes all the diffusive and boundary layer effects, and b is the total buoyancy force defined in Eq. (5) where the mean virtual temperature $\hat{T}_v(z)$ is obtained from the hydrostatic equation using $\overline{p}(z, t)$. To obtain the basic-state pressure at time t, we choose a square of 36 km on a side centered 138 km northeast of the storm (representing roughly the storm environment). The basic-state pressure $\overline{p}(z, t)$ represents the horizontally averaged model pressure over the square.

Unlike previous cloud modeling studies (Rotunno and Klemp 1982; Schlesinger 1984), we did not simplify Eq. (A1) using the basic-state density [i.e., $\hat{\rho}(z)$] because the density of air varies significantly with radius and altitude in the inner-core region of hurricanes.

Applying "$\nabla\cdot$" to Eq. (A1) yields

$$\nabla^2 P' = \frac{\partial \rho b}{\partial z} - \nabla\cdot(\rho\mathbf{V}\cdot\nabla\mathbf{V}) - 2\nabla\cdot(\rho\boldsymbol{\Omega}\times\mathbf{V}) + \nabla\cdot(\rho\mathbf{D}_v), \quad \text{(A2)}$$

where the first term on the rhs is referred to as the buoyancy source (F_b) and the remaining three terms as the dynamic source (F_d). In deriving Eq. (A2), we have neglected the local tendency of $\nabla\cdot\mathbf{V}$ because its magnitude is very small relative to other terms during the mature stage of the hurricane. Assuming that all the rhs terms are known, and given proper boundary conditions, P' could be inverted from the three-dimensional Poisson equation (A2).

The inversion of Eq. (A2) is carried out using the routine MUDPACK 4.0 on NCAR's Cray Y-MP (see Adams 1993 for more details). To validate the accuracy of MUDPACK, we performed a preliminary inversion by specifying all the source terms on the rhs using a horizontal grid size of 6 km and a vertical grid size of 120 m. For this test case, we use a Dirichlet-type boundary condition by specifying the model-calculated perturbation pressure at the top–bottom and lateral boundaries. It was found that when the P' obtained from the inversion is azimuthally averaged, it deviates from p'_2 (Fig. 1a) by no more than 0.1 hPa (not shown). The maximum difference occurs at an altitude of 7.5 km in the eye where the warm core reaches its maximum value.

As mentioned in section 4, we are mainly interested in the relative importance of the buoyancy- and dynamically induced PGF in the development of vertical motion in hurricanes. However, we have little information to specify the individual *buoyancy and dynamic perturbation pressures* at the boundaries. As a first attempt, we follow Rotunno and Klemp (1982) by specifying the

individual *perturbation pressure gradients* normal to the boundaries (the so-called Neumann-type boundary conditions). Specifically, we applied Eq. (A1) by ignoring the local momentum tendency and eliminating those terms which do not contribute to the pressure gradient normal to the boundaries. However, the results were not satisfactory as the azimuthally averaged inverted P' has a maximum error of about 0.8 hPa in the vicinity of $V_{\max}$ (not shown) when compared to p'_2.

Further experimentation was made and it was found that the following procedure and boundary conditions resulted in a more accurate solution. First, we extend the inversion domain from 360 km × 360 km to 480 km × 480 km and set the buoyancy source to zero in the extended region. Second, the boundary conditions for inverting the buoyancy-induced perturbation pressure P_b are specified as

$$P_b|_x = 0;$$

$$P_b|_y = 0 \quad \text{for lateral boundaries in } x \text{ and } y, \quad \text{and}$$

$$\partial P_b/\partial z = \rho b \quad \text{for top and bottom boundaries.} \qquad \text{(A3)}$$

By invoking (A3), the inverted P_b can be determined uniquely, which is unlike the case of the Neumann boundary conditions where P_b can only be determined within an arbitrary constant.

Similarly, the dynamic sources are set to zero in the extended region when inverting the dynamically induced P_d. The boundary conditions are

$$P_d|_x = 0;$$

$$P_d|_y = 0 \quad \text{for lateral boundaries at } x \text{ and } y, \quad \text{and}$$

$$\partial P_d/\partial z = \rho(U\partial W/\partial x + V\partial W/\partial y + W\partial W/\partial z) + 2\rho\Omega u \cos\phi + \rho D_w \quad \text{for top and bottom boundaries.} \qquad \text{(A4)}$$

Figures 7a,b depict the azimuthally averaged inverted P_b and P_d, respectively. The difference field between the azimuthally averaged inverted P' and the model-derived p'_2 (shown in Fig. 1a) is given in Fig. 7c. The errors in the inner-core region are very small, ranging from 0.1 to −0.2 hPa. Even though the radial gradients in P_b and P_d are large, the radial gradient of P' ($=P_b + P_d$) nearly vanishes at the model top, as is the radial gradient of p'_2. Our results therefore show that our methodology for obtaining the PGFs are sufficiently accurate to allow an analysis of the relative importance of the dynamic and buoyancy forces in the development of secondary circulations in the inner-core region of the hurricane.

REFERENCES

Adams, J., 1993: MUDPACK-2: Multigrid software for approximating elliptic partial differential equations on uniform grids with any resolution. *Appl. Math. Comput.,* **53,** 235–249.

Anthes, R. A., 1972: The development of asymmetries in a three-dimensional numerical model of the tropical cyclone. *Mon. Wea. Rev.,* **100,** 461–476.

Black, R. A., H. B. Bluestein, and M. L. Black, 1994: Unusually strong vertical motions in a Caribbean hurricane. *Mon. Wea. Rev.,* **122,** 2722–2739.

Dudhia, J., 1993: A nonhydrostatic version of the Penn State–NCAR mesoscale model: Validation tests and simulation of an Atlantic cyclone and cold front. *Mon. Wea. Rev.,* **121,** 1493–1513.

Ebert, E. E., and G. J. Holland, 1992: Observations of record deep convection in Tropical Cyclone Hilda. *Mon. Wea. Rev.,* **120,** 2240–2251.

Emanuel, K. A., 1986: An air–sea interaction theory for tropical cyclones. Part I: Steady–state maintenance. *J. Atmos. Sci.,* **43,** 585–604.

——, 1997: Some aspects of hurricane inner-core dynamics and energetics. *J. Atmos. Sci.,* **54,** 1014–1026.

Gray, W. M., and D. J. Shea, 1973: The hurricanes inner core region: Thermal stability and dynamic characteristics. *J. Atmos. Sci.,* **30,** 1565–1576.

Grell, G. A., J. Dudhia, and D. R. Stauffer, 1995: A description of the fifth generation Penn State/NCAR mesoscale model (MM5). NCAR Tech Note NCAR/TN-398+STR, 138 pp.

Jorgenson, D. P., E. J. Zipser, and M. A. LeMone, 1985: Vertical motion in intense hurricanes. *J. Atmos. Sci.,* **42,** 839–856.

Klemp, J. B., and R. Rotunno, 1983: A study of the tornadic region within a supercell thunderstorm. *J. Atmos. Sci.,* **40,** 359–377.

Kuo, H.-L., 1959: Dynamics of convective vortices and eye formation. *The Atmosphere and Sea in Motion,* B. Bolin, Ed., Rockefeller Institute Press, 413–424.

Kurihara, Y., and R. E. Tuleya, 1981: A numerical simulation study on the genesis of a tropical storm. *Mon. Wea. Rev.,* **109,** 1629–1653.

Liu, Y., D.-L. Zhang, and M. K. Yau, 1997: A Multiscale numerical study of Hurricane Andrew (1992). Part I: An explicit simulation. *Mon. Wea. Rev.,* **125,** 3073–3093.

——, ——, and ——, 1999: A multiscale numerical study of Hurricane Andrew (1992). Part II: Kinematics and inner-core structures. *Mon. Wea. Rev.,* **127,** 2597–2616.

Malkus, J. S., 1958: On the structure and maintenance of the mature hurricane eye. *J. Meteor.,* **15,** 337–349.

Ooyama, K., 1969: Numerical simulation of the life cycle of tropical cyclones. *J. Atmos. Sci.,* **26,** 3–40.

Rotunno, R., and J. B. Klemp, 1982: The influence of the shear-induced pressure gradient on thunderstorm motion. *Mon. Wea. Rev.,* **110,** 136–151.

——, and K. A. Emanuel, 1987: An air–sea interaction theory for tropical cyclones. Part II: Evolutionary study using a nonhydrostatic axisymmetric numerical model. *J. Atmos. Sci.,* **44,** 542–561.

Schlesinger, R. E., 1984: Effects of the pressure perturbation field in numerical models of unidirectionally sheared thunderstorm convection: Two versus three dimensions. *J. Atmos. Sci.,* **41,** 1571–1587.

Shapiro, L. J., and H. E. Willoughby, 1982: The response of balanced hurricanes to local sources of heat and momentum. *J. Atmos. Sci.,* **39,** 378–394.

Smith, R. K., 1980: Tropical cyclone eye dynamics. *J. Atmos. Sci.,* **37,** 1227–1232.

Willoughby, H. E., 1990: Gradient balance in tropical cyclones. *J. Atmos. Sci.,* **47,** 265–274.

——, 1998: Tropical cyclone eye thermodynamics. *Mon. Wea. Rev.,* **126,** 3053–3067.

Zhang, D.-L., Y. Liu, and M. K. Yau, 1999: Surface winds at landfall of Hurricane Andrew (1992)—A reply. *Mon. Wea. Rev.,* **127,** 1711–1721.